Supporting Information

Green Synthesis of Heterolayered 2D Nanohybrid Catalytic Hydrogel Cell for Environmental-Friendly Water Splitting

Seonmyeong Noh,[b] Thanh-Hai Le,[b] Changjun Kim,[b] Minseong Ju,[b] Haney Lee,[b]
S. K. Nataraj[a,c,*] and Hyeonseok Yoon[a,b,*]

[a]School of Polymer Science and Engineering, Chonnam National University,
77 Yongbong-ro, Buk-gu, Gwangju 61186, South Korea.
E-mail: hyoon@chonnam.ac.kr; Fax: +82-62-530-1779; Tel: +82-62-530-1778
[b]Department of Polymer Engineering, Graduate School, Chonnam National University,
77 Yongbong-ro, Buk-gu, Gwangju 61186, South Korea.
[c]Centre for Nano and Material Sciences, Jain University, Jain Global Campus, Kanakapura,
Ramanagaram, Bangalore 562112, India

KEYWORDS: Liquid-phase exfoliation; 2D materials; nanohybrids; electrocatalysts; hydrogel water splitting cell

Additional experimental section

Density functional theory calculations. Density functional theory (DFT) calculations of the BMHNs and controls were carried out using the ORCA 5.0.2 program with Avogadro software.[1-3] Gibbs free-energy of the BMHNs and controls were calculated based on the analytical frequency calculation method using the BP86 functional with def2-SVP and def2/J basis sets.[4-6] Note that the calculations were utilized based on a computational hydrogen electrode model with no external bias ($U = 0$) and standard conditions ($T = 298.15$ K and $P = 1$ atm).[7,8] The Gibbs free-energy change (ΔG) can be written as:

$$\Delta G = \Delta E + \Delta E_{\text{ZPE}} - T\Delta S$$

where ΔE, ΔE_{ZPE}, and ΔS are the net total energy, net zero-point, and the net entropy change between reactant and product states, respectively, T is the temperature. For the HER calculations, the free energy of hydrogen adsorption of a catalyst (ΔG_{H}) can be calculated using the following equation:

$$\Delta G_{\text{H}*} = \Delta E_{\text{H}*} + \Delta E_{\text{ZPE}} - T\Delta S_{\text{H}},$$
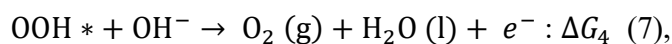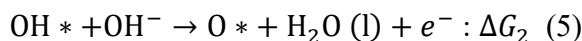
in which $\Delta E_{\text{H}*}$ and ΔE_{ZPE} refer to the net adsorption energy and net zero-point energy, respectively, are described as:

$$\Delta E_{\text{H}*} = E[\text{H} *] - E[*] - \frac{1}{2}E[\text{H}_2],$$

and

$$\Delta E_{\text{ZPE}} = E_{\text{ZPE}}^{\text{H}*} - E_{\text{ZPE}}^{*} - \frac{1}{2}E_{\text{ZPE}}^{\text{H}_2},$$

where $E[\text{H} *]$, $E[*]$, and $E[\text{H}_2]$ indicate the total energy of an absorbed hydrogen atom on the nanohybrids, the total energy of the clean nanohybrids, and the total energy of a gas-phase H_2 molecule, respectively; $E_{\text{ZPE}}^{\text{H}*}$ and E_{ZPE}^{*} define the zero-point energies of an absorbed hydrogen atom on the nanohybrids and the clean hybrids, respectively; and $E_{\text{ZPE}}^{\text{H}_2}$ describes the zero-point energy of gas-phase hydrogen (298.15 K, 1 bar). For the OER calculations, the four elementary steps and their free-energy changes are expressed as:

$$\text{OH}^- + * \rightarrow \text{OH} * + e^- : \Delta G_1 \text{ (4)}$$

$$\text{OH} * + \text{OH}^- \rightarrow \text{O} * + \text{H}_2\text{O (l)} + e^- : \Delta G_2 \text{ (5)}$$

$$\text{O} * + \text{OH}^- \rightarrow \text{OOH} * + e^- : \Delta G_3 \text{ (6)}$$

$$\text{OOH} * + \text{OH}^- \rightarrow \text{O}_2 \text{ (g)} + \text{H}_2\text{O (l)} + e^- : \Delta G_4 \text{ (7)},$$

where ΔG_1, ΔG_2, ΔG_3, and ΔG_4 identify $\Delta G_{\text{OH}*}$, $\Delta G_{\text{O}*} - \Delta G_{\text{OH}*}$, $\Delta G_{\text{OOH}*} - \Delta G_{\text{O}*}$, and 4.92 (eV) $- \Delta G_{\text{OOH}*}$, respectively. The values ΔE for the absorbed molecules are calculated based on the following equations:

$$\Delta E_{\text{OH}*} = E[\text{OH} *] - E[*] - \left(E[\text{H}_2\text{O}] - \frac{1}{2}E[\text{H}_2]\right)$$

$$\Delta E_{O*} = E[O*] - E[*] - (E[H_2O] - E[H_2])$$

$$\Delta E_{OOH*} = E[OOH*] - E[*] - \left(2E[H_2O] - \frac{3}{2}E[H_2]\right)$$

Similarly, ΔE_{ZPE} and ΔS are calculated under the same conditions as the calculation for HER.

The theoretical overpotentials for the OER is defined as:

$$\eta^{theory}{}_{\_OER} = \frac{\max(\Delta G_1, \ \Delta G_2, \ \Delta G_3, \ \Delta G_4)}{e} - 1.23 \ (V)$$
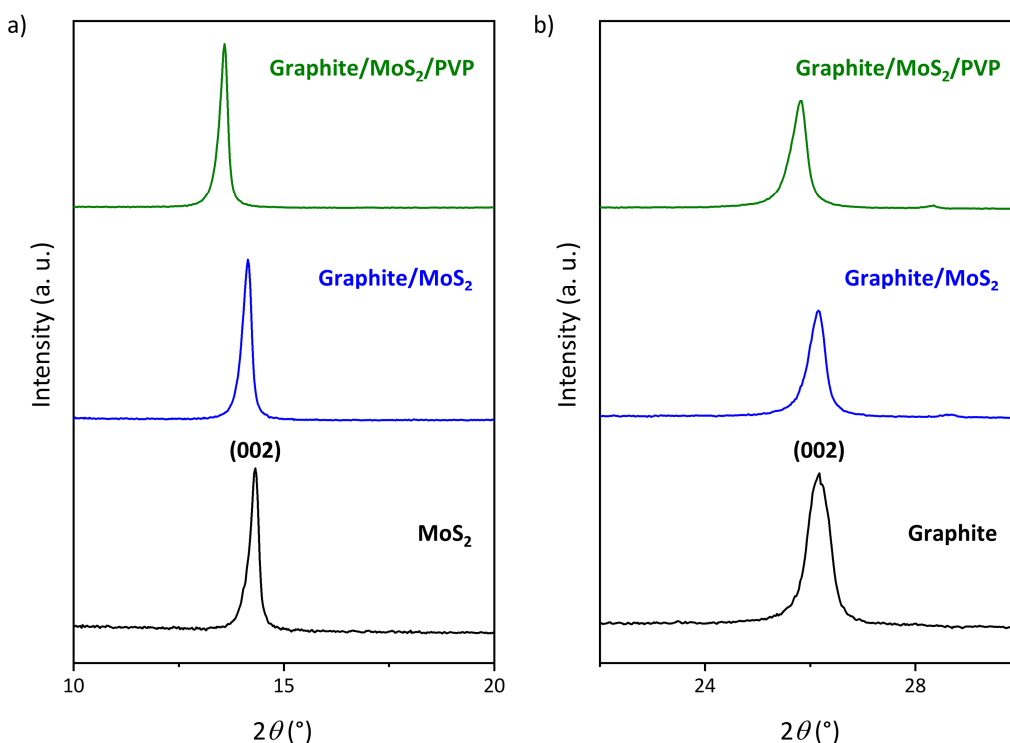
Figure S1. X-ray diffraction patterns of the combination of graphite, MoS_2, and PVP: (002) refractions of a) MoS_2 and b) graphite.

To estimate the layer spacing of 2D materials, (002) reflection in the XRD patterns was investigated, as presented in Figure S1. The (002) reflection peaks of MoS_2 and graphite were located at 14.320 and 26.176 °, respectively, which are consistent with 14.378 (JCPDS card no. 37−1492) and 26.228 ° (JCPDS card no. 75−1621), respectively. The layer spacings of graphite and MoS_2 were calculated using the following equation:

$$n\lambda = 2d\sin\theta$$

where n is the diffraction order ($n = 1$ for (002) reflections of MoS_2 and graphite), λ is the wavelength (1.5418 Å), d is the spacing of the crystal layers, and θ is the incident angle, respectively. The calculated d values of MoS_2 and graphite were determined to be 0.62 and 0.34 nm, respectively, which are reasonably consistent with the reported values in the literature.[9,10] The d values of graphite/MoS_2 were calculated to be 0.63 and 0.34 nm for MoS_2 and graphite layers,

respectively, while the d values of graphite/MoS$_2$/PVP were determined to be 0.65 and 0.35 nm for MoS$_2$ and graphite layer, respectively, demonstrating that PVP facilitates the co-exfoliation of 2D materials.
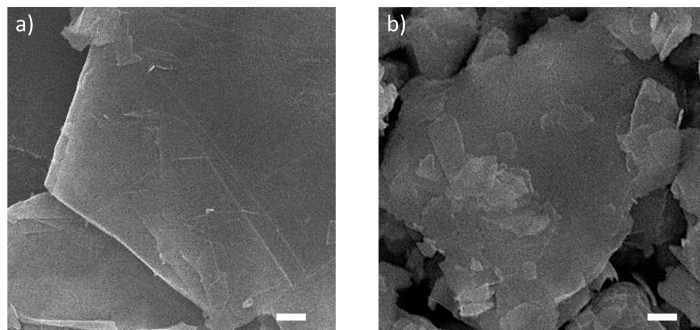
Figure S2. SEM images of a) graphite flake and b) bulk MoS_2 (scale bar: 500 nm).
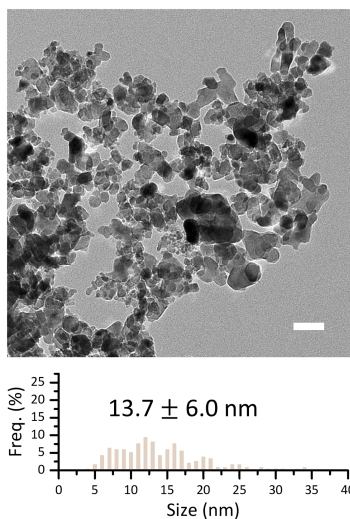
Figure S3. TEM images of NF (NiFe$_2$O$_4$) nanoparticles with size distribution histogram (scale bar: 50 nm).
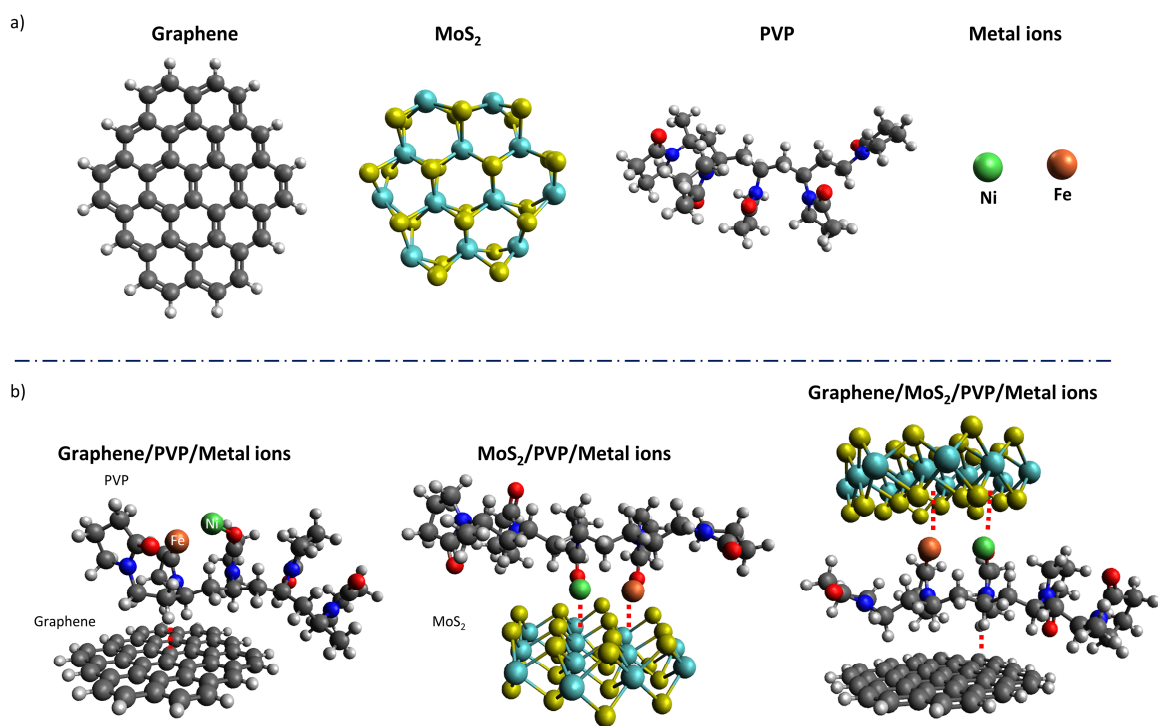
Figure S4. DFT calculations of the miniature models for the BMNHs: a) the miniature models of components and b) optimized geometrical structures.

DFT calculations for the optimized geometrical structure were carried out using the miniature models (Figure S4). Figure S4b shows the three different combinations: Graphene/PVP/metal ions, MoS_2/PVP/metal ions, and Graphene/MoS_2/PVP/metal ions. From these results, the transition metal ions are favorable to closely locate near MoS_2 due to strong interactions between the transition metal ion and MoS_2, which is consistent with the reported literature.[11,12]
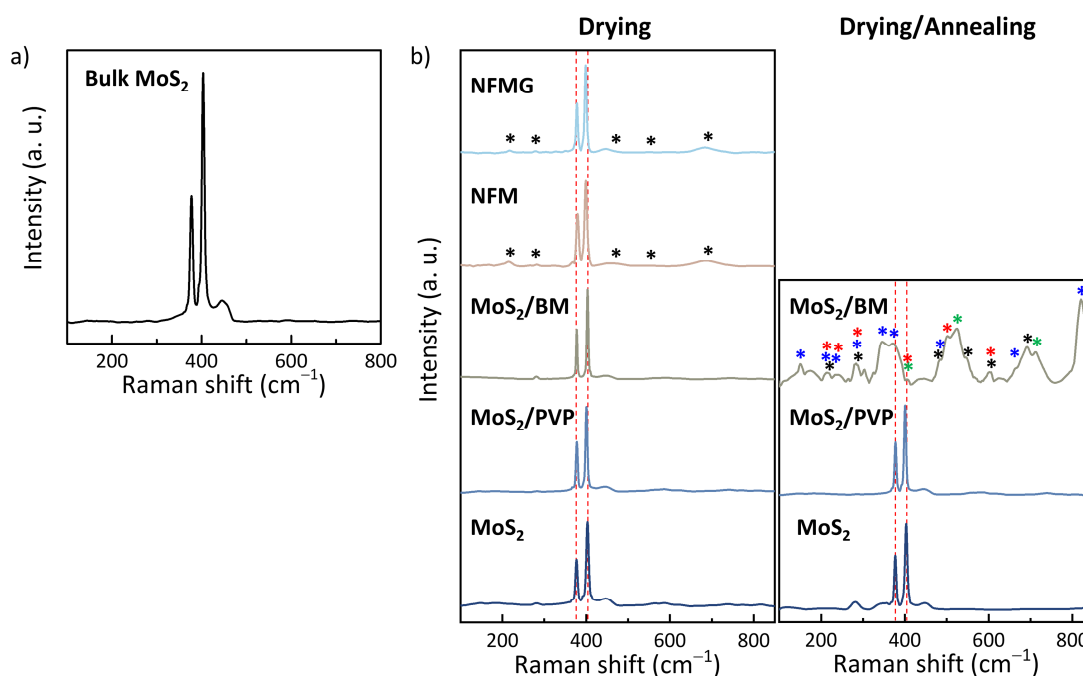
Figure S5. Raman spectra of a) bulk MoS_2 and b) BMNHs and combinations (left: drying and right: drying/annealing, with 532 nm excitation (asterisk: black ($NiFe_2O_4$), green (NiO),[13] red (Fe_2O_3),[14] and blue (MoO_3),[15] and red dash line: MoS_2 peaks).

To further investigate the conversion of 2H-MoS_2 to 1T-MoS_2, Raman spectroscopy was utilized for the MoS_2-based combinations after the drying or drying/annealing process, as seen in Figure S5b. During the drying process, a few $NiFe_2O_4$ nanoparticles were formed in NFMG and NFM, but no phase conversion from 2H-MoS_2 to 1T-MoS_2 occurred. Moreover, it was revealed that the phase conversion of 2H-MoS_2 to 1T-MoS_2 was not achieved in the absence of PVP or the transition metal ions. In the absence of PVP, the E^1_{2g} and A_{1g} modes for the MoS_2 overlapped with the peaks of the metal oxide derivatives after the drying/annealing process, which was attributed to the strong interactions between transition metal ions and MoS_2 as well as the residual ethanol (i.e., oxygen precursor) in the hybrids. In addition, the formation of the metal oxide derivatives destroyed the S edge in MoS_2, resulting in the formation of MoO_3 in the nanohybrids.[16] On the other hand, in the absence of metal ions, the no corresponding peaks of 1T-MoS_2 were observed in the spectrum of MoS_2/PVP despite the red shift of the A_{1g} peak after

the drying/annealing process. Thus, it can be concluded that the phase conversion of $2H\text{-}MoS_2$ to $1T\text{-}MoS_2$ is achieved in the presence of metal cations and PVP through the drying/annealing process.
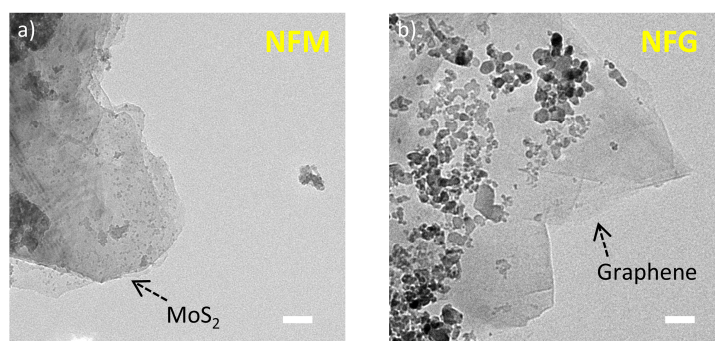
Figure S6. Analysis of layer numbers in the BMNHs: TEM images of a) NFM and b) NFM (scale bar: 50 nm).

Figure S6 shows the TEM images of the MoS_2 layers and graphite layers in the NFM and NFG, respectively. Note that the similar shape of graphene sheets to MoS_2 sheets made it difficult to distinguish graphene and MoS_2 sheets through TEM analysis. Nevertheless, owing to the calculated 2D layer numbers of NFM and NFG similar to those of NFMG, we were able to select both NFM and NFG to visually observe the MoS_2 and graphite layer numbers in the BMNHs. The MoS_2 and graphite layers were determined to be approximately 3, as shown in Figure S6, which is consistent with the calculated results in Figure 4a and 4b. Thus, these results support that few-layered constituent 2D materials in the nanohybrids.
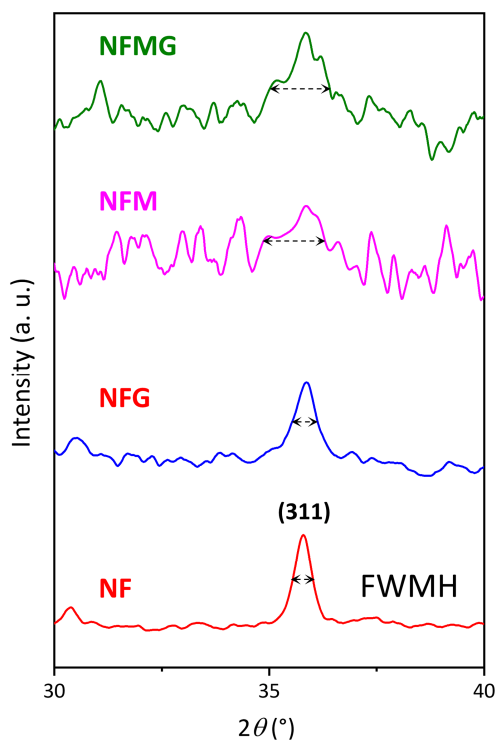
Figure S7. X-ray diffraction patterns of (311) reflection of $NiFe_2O_4$ in the BMNHs.

To estimate the crystalline size of $NiFe_2O_4$ in the BMHNs, XRD analysis was carried out (Figure S7). The crystalline size (D) of $NiFe_2O_4$ particles in the BMNHs was calculated using the Scherrer equation.

$$D = \frac{K\lambda}{\beta\cos\theta}$$

in which K is a crystalline-shape factor (i.e., 0.9), λ is the wavelength (1.5418 Å), β is the width (full-width at half-maximum) of the corresponding diffraction peak, and θ is the Bragg angle, respectively. The representative peak at 35.7° was assigned to (311), which was selected to calculate D of the BMNHs. The D values increased in the order of NFM (5.84 nm) < NFMG (6.30 nm) < NFG (13.97 nm) < NF (16.98 nm), which is similar to the measured particle sizes in TEM images.

Table S1. Equivalent circuit component values of BMHNs calculated by fitting the EIS plots in Figure 5c.
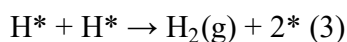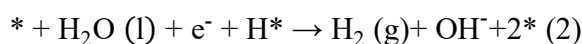
Sample	R_s (Ω)	R_{ct} (Ω)	C_{dl} (μF)
NFMG	11.8	7.3	188.2
NFM	11.9	11.5	144.8
NFG	12.3	39.9	49.9
NG	12.0	23.4	39.5

Table S2. Equivalent circuit component values of BMHNs calculated by fitting the EIS plots in Figure 5f.

Sample	R_s (Ω)	R_{ct} (Ω)	C_{dl} (μF)
NFMG	12.0	4.1	323.5
NFM	11.7	32.0	166.1
NFG	11.8	8.1	244.5
NF	11.8	129.2	134.9

Investigation of HER mechanism using Tafel slope

In alkaline media, HER follows three different reaction steps.

$$* + H_2O \text{ (l)} + e^- \rightarrow H* + OH^- \text{ (1)}$$

$$* + H_2O \text{ (l)} + e^- + H* \rightarrow H_2 \text{ (g)} + OH^- + 2* \text{ (2)}$$

$$H* + H* \rightarrow H_2\text{(g)} + 2* \text{ (3)}$$
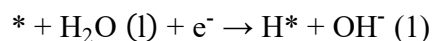
where * is the active site on a catalyst. The reaction steps, (1), (2), and (3), correspond to the Volmer, Heyrovsky, and Tafel mechanisms, respectively. Tafel slope is expressed as follows:

$$\text{Tafel slope} = \frac{2.303\ RT}{\alpha z F}$$

where R is the gas constant, T is the room temperature, α is the transfer coefficient (i.e., 0.5), z is the number of electrons transferred in the reaction, and F is the Faraday's constant (96485 C mol^{-1}). In particular, z consists of the number of electron transfers before (z_b) and during the rate-determining step (RDS) (z_r) in the Tafel slope, which can be modified as follows:[17]

$$\text{Tafel slope} = \frac{60\ m\ Vdec^{-1}}{z_b + \frac{z_r}{2}}$$

The calculated z_b, z_r, and corresponding Tafel slopes were summarized in Table S3. The Tafel slope of NFMG, NFM, NFG, and NF were determined to be 78.8, 106.0, 114.8, and 139.7 mV dec^{-1}, as shown in Figure 5b. Based on these results, the RDS of NFMG is the Volmer−Heyrovsky mechanism, while the RDS of NFM, NFG, and NF is Volmer mechanism.[18,19]

Table S3. Number of electron transfers before and during the RDS in the HER, and corresponding Tafel slopes.

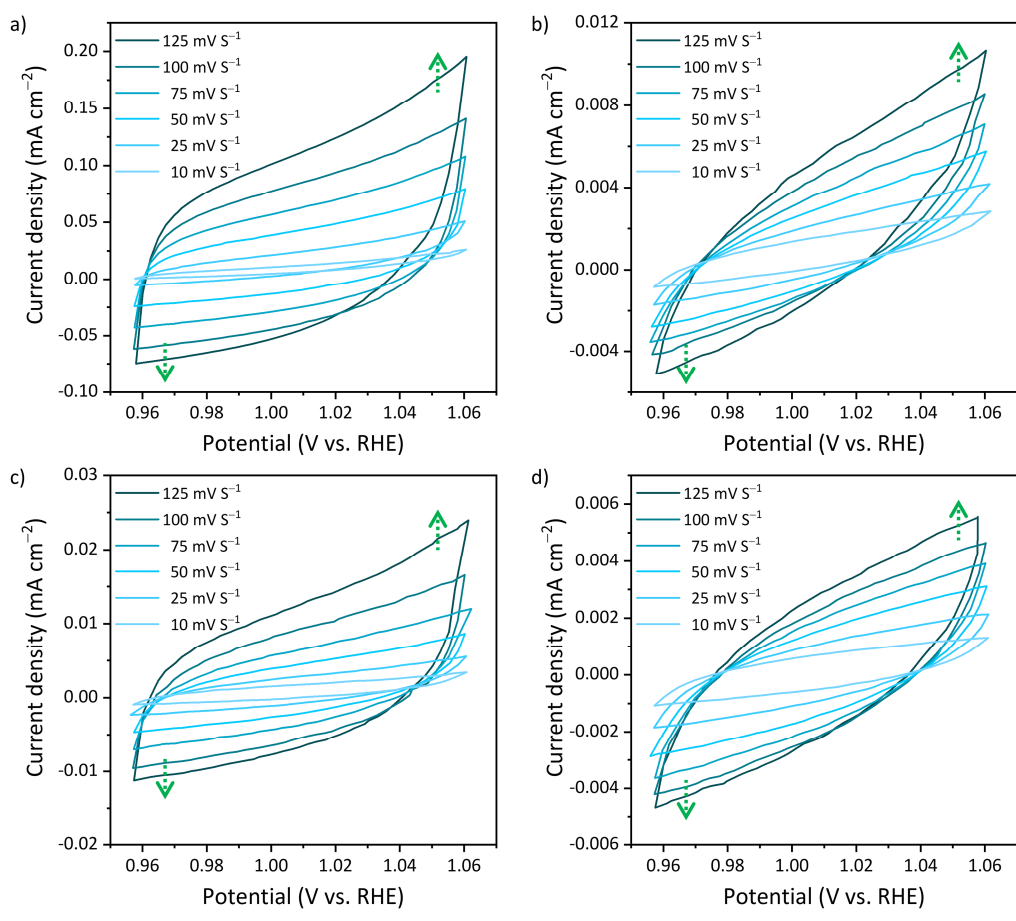| Mechanism	Z_b	Z_r	Tafel slope (mV dec^{-1})
Volmer	0	1	120
Heyrovsky	1	1	40
Tafel	2	0	30

Figure S8. CV curves recorded at different scan rates in 1 M KOH: a) NFMG, b) NFM, c) NFG, and d) NF.

Estimation of the ECSA corrected current density

Estimation of the impact of surface area of the BMNHs in electrocatalytic performance in the HER and OER, respectively, was carried out. First, electrochemically active surface area (ECSA) was calculated using the following equation.[20]

$$\text{ECSA} = \frac{C_{dl}}{C_s}$$

where C_{dl} is the electrochemical double layer capacitance and C_s is the specific capacitance, respectively. In general, the value of C_s is assumed to be 0.04 mF cm^{-2} in 1 M KOH.[21]

$$C_{dl} = \frac{j_c}{v}$$

in which j_c is the charging current density, and v is the scan rate, respectively. Note that the value of C_{dl} were obtained from Figure 6a. The calculated ECSA of the BMNHs were summarized in Table S3. Next, the current density with ECSA correction, j_{ECSA} was expressed as follows.[22]

$$j_{ECSA} = \frac{j}{\text{ECSA}}$$

Figure S9 shows the ECSA corrected j of the BMNHs for the HER and OER. The electrocatalytic performance of NFMG is outstanding compared to other BMNHs. However, these results are not convincing due to the following two reasons: i) Not all electrochemically active sites provide electrocatalytic active sites for HER and OER. ii) Even though graphite behavior as a non-faradaic reaction increases in C_{dl} value, it results in poor electrocatalytic performance in HER and OER, as seen in Figure S10, which leads to a higher C_{dl} value compared to the actual C_{dl} value for the HER and OER. Considering the limitations of the use of j_{ECSA}, it was not able to use the current density with ECSA correction. Therefore, it was decided to use the geometric area unit to calculate a current density for the electrocatalytic data.

Table S4. ECSA values of the BMNHs calculated using the C_{dl} in Figure 6a.

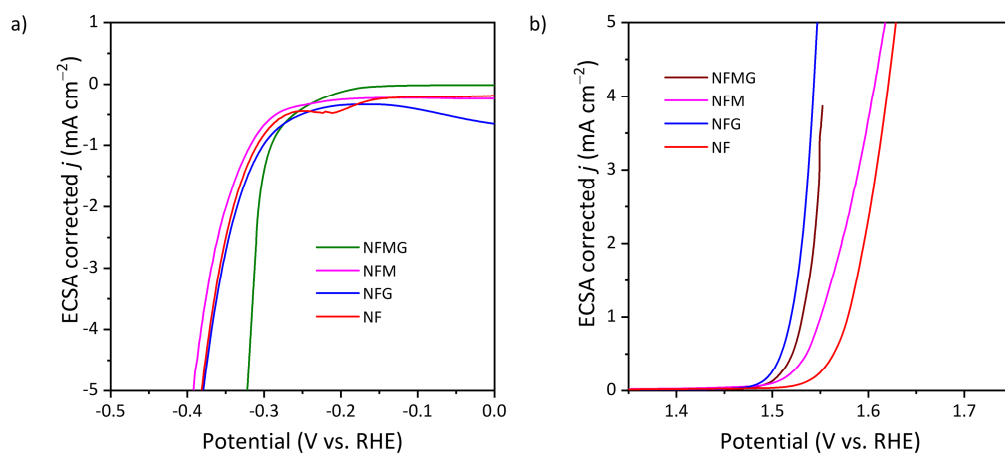| Sample	ECSA
NFMG	33.5
NFM	3.8
NFG	1.1
NF	0.8

Figure S9. LSV curves with ECSA correction recorded at a scan rate of 10 mV s^{-1} in 1.0 M KOH: a) HER and b) OER.
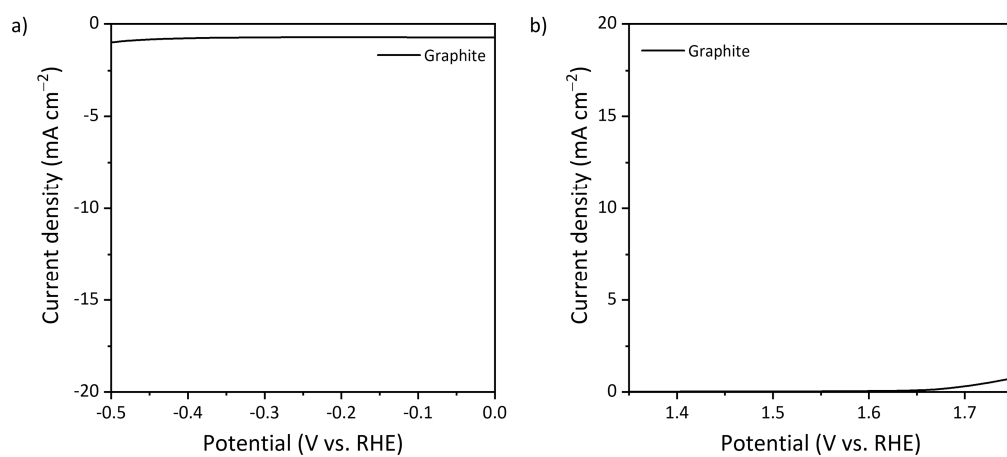
Figure S10. LSV curves of graphite recorded at a scan rate of 10 mV s^{-1} in 1.0 M KOH: a) HER and b) OER.

Table S5. Summary of the catalytic performance of the BMHNs and other electrocatalysts for the HER and OER shown in Figure 6c.

| Sample	η_{HER} (mV)	*Ref*	Sample	η_{OER} (mV)	*Ref*
Pt/C	35	This work	GMBT	283	This work
NFMG	234	This work	RuO_2	295	This work
NFM	363	This work	NFG	331	This work
NFG	411	This work	NFM	354	This work
NF	417	This work	NF	455	This work
$NiFe_2O_4$	264	23	$NiO/NiFe_2O_4$ nanorods	302	31
$Ni_{1.5}Fe_{0.5}P$	282	24	mesoporous $NiO/NiFe_2O_4$	303	32
$NiFe_2O_4$	300	25	$C_{NF}SPNF$	327	33
NiFe LDH-NS@DG10	300	26	$NiFe_2O_4$ nanotubes	340	34
NiP_2-FeP_2/CFP	323	27	$NiFe_2O_4/NF$	343	35
Ni-Fe LDH(60%)/MX-RGO	326	28	$NiFe_2O_4-H_2$	389	36
$C_{NF}SPNF$	329	29	3DOM-$NiFe_2O_4$powder/CC	404	37
$NiFe_2O_4$	412	30	Mesoporous $NiFe_2O_4$	410	38

HER   OER
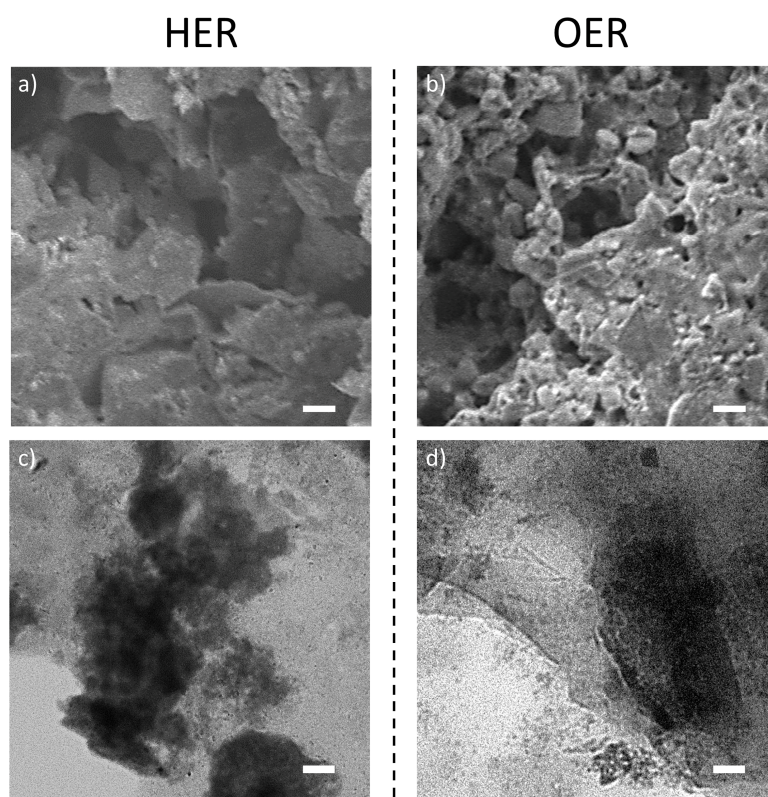
Figure S11. Analysis of morphology of NFMG after water splitting at an applied potential of 1.79 V for 24 h: (a,b) SEM and (c,d) TEM images of NFMGs for (a,c) HER and (b,d) OER, respectively (scale bar: 500 nm and 50 nm for SEM and TEM images, respectively). After the electrolysis, dried NFMGs under vacuum to remove the residual electrolyte were analyzed.

References

(1) Neese, F. The ORCA program system. *WIREs Comput. Mol. Sci.* **2012**, *2*, 73−78.

(2) Neese, F. Software update: The ORCA program system—Version 5.0. *WIREs Comput. Mol. Sci* **2022**, *12*, e1606.

(3) Hanwell, M. D.; Curtis, D. E.; Lonie, D. C.; Vandermeersch, T.; Zurek, E.; Hutchison, G. R. Avogadro: an advanced semantic chemical editor, visualization, and analysis platform. *J. Cheminform.* **2012**, *4*, 17.

(4) Perdew, J. P. Density-functional approximation for the correlation energy of the inhomogeneous electron gas. *Phys. Rev. B* **1986**, *33*, 8822−8824.

(5) Becke, A. D. Density-functional exchange-energy approximation with correct asymptotic behavior. *Phys. Rev. A* **1988**, *38*, 3098−3100.

(6) Weigend, F.; Ahlrichs, R. Balanced basis sets of split valence, triple zeta valence and quadruple zeta valence quality for H to Rn: Design and assessment of accuracy *Phys. Chem. Chem. Phys.* **2005**, *7*, 3297−3305.

(7) Nørskov, J. K.; Rossmeisl, J.; Logadottir, A.; Lindqvist, L.; Kitchin, J. R.; Bligaard, T.; Jónsson, H. Origin of the overpotential for oxygen reduction at a fuel-cell cathode. *J. Phys. Chem. B* **2004**, *108*, 17886−17892.

(8) Peterson, A. A.; Abild-Pedersen, F.; Studt, F.; Rossmeisl, J.; Nørskov, J. K. How copper catalyzes the electroreduction of carbon dioxide into hydrocarbon fuels. *Energy Environ. Sci.* **2010**, *3*, 1311−1315.

(9) Kim, T.-H.; Jeon, E. K.; Ko, Y.; Jang, B. Y.; Kim, B.-S.; Song, H.-K., Enlarging the d-spacing of graphite and polarizing its surface charge for driving lithium ions fast. *J. Mater. Chem. A* **2014**, *2*, 7600−7605.

(10) Hu, L.; Ren, Y.; Yang, H.; Xu, Q., Fabrication of 3D hierarchical MoS_2/polyaniline and MoS_2/C architectures for lithium-ion battery applications. *ACS Appl Mater Interfaces* **2014**, *6*, 14644−14652.

(11) Fan, Y.; Zhang, J.; Qiu, Y.; Zhu, J.; Zhang, Y.; Hu, G., A DFT study of transition metal (Fe, Co, Ni, Cu, Ag, Au, Rh, Pd, Pt and Ir)-embedded monolayer MoS_2 for gas adsorption. Computational Materials Science **2017**, *138*, 255−266.

(12) Mo, J.; Wu, S.; Lau, T. H. M.; Kato, R.; Suenaga, K.; Wu, T. S.; Soo, Y. L.; Foord, J. S.; Tsang, S. C. E., Transition metal atom–doped monolayer MoS_2 in a proton-exchange membrane electrolyzer. *Mater. Today Adv.* **2020**, *6*, 100020.

(13) Faid, A. Y.; Barnett, A. O.; Seland, F.; Sunde, S., Ni/NiO nanosheets for alkaline hydrogen evolution reaction: In situ electrochemical-Raman study. *Electrochim. Acta* **2020**, *361*, 137040.

(14) Li, H.; Wan, J.; Ma, Y.; Wang, Y., Synthesis of novel core–shell $Fe^0@Fe_3O_4$ as heterogeneous activator of persulfate for oxidation of dibutyl phthalate under neutral conditions. *Chem. Eng. J.* **2016**, *301*, 315−324.

(15) Ou, J. Z.; Campbell, J. L.; Yao, D.; Wlodarski, W.; Kalantar-zadeh, K., In situ Raman spectroscopy of H_2 gas interaction with layered MoO_3. *J. Phys. Chem. C* **2011**, *115*, 10757−10763.

(16) Reidy, K.; Mortelmans, W.; Jo, S. S.; Penn, A. N.; Foucher, A. C.; Liu, Z.; Cai, T.; Wang, B.; Ross, F. M.; Jaramillo, R., Atomic-scale mechanisms of MoS_2 oxidation for kinetic control of MoS_2/MoO_3 interfaces. *Nano Lett.* **2023**, *23*, 5894−5901.

(17) Watkins, N. B.; Schiffer, Z. J.; Lai, Y.; Musgrave, C. B., III; Atwater, H. A.; Goddard, W. A., III; Agapie, T.; Peters, J. C.; Gregoire, J. M., Hydrodynamics change Tafel slopes in electrochemical CO_2 Reduction on copper. *ACS Energy Lett.* **2023**, *8*, 2185−2192.

(18) Peng, L.; Liang, Y.; Wu, S.; Li, Z.; Sun, H.; Jiang, H.; Zhu, S.; Cui, Z.; Li, L., Nanoporous Ni/NiO catalyst for efficient hydrogen evolution reaction prepared by partial electro-oxidation after dealloying. *J. Alloys Compd.* **2022**, *911*, 165061.

(19) Chen, Z.; Hu, H.; Yin, L.; Zhao, Z.; Choi, J.-H.; Liu, G.; Geng, F., Composite non-noble system with bridging oxygen for catalyzing Tafel-type alkaline hydrogen evolution. *Proc. Natl. Acad. Sci. U. S. A.* **2023**, *120*, e2209760120.

(20) McCrory, C. C.; Jung, S.; Peters, J. C.; Jaramillo, T. F., Benchmarking heterogeneous electrocatalysts for the oxygen evolution reaction. *J. Am. Chem. Soc.* **2013**, *135*, 16977−16987.

(21) Browne, M. P.; Nolan, H.; Duesberg, G. S.; Colavita, P. E.; Lyons, M. E. G., Low-overpotential high-activity mixed manganese and ruthenium oxide electrocatalysts for oxygen evolution reaction in Aalkaline media. *ACS Catal.* **2016**, *6*, 2408−2415.

(22) Voiry, D.; Chhowalla, M.; Gogotsi, Y.; Kotov, N. A.; Li, Y.; Penner, R. M.; Schaak, R. E.; Weiss, P. S., Best practices for reporting electrocatalytic performance of nanomaterials. *ACS Nano* **2018**, *12*, 9635−9638.

(23) Maruthapandian, V.; Mathankumar, M.; Saraswathy, V.; Subramanian, B.; Muralidharan, S. Study of the oxygen evolution reaction catalytic behavior of $Co_xNi_{1-x}Fe_2O_4$ in alkaline medium. *ACS Appl. Mater. Interfaces* **2017**, *9*, 13132−13141.

(24) Huang, H.; Yu, C.; Zhao, C.; Han, X.; Yang, J.; Liu, Z.; Li, S.; Zhang, M.; Qiu, J. Iron-tuned super nickel phosphide microstructures with high activity for electrochemical overall water splitting. *Nano Energy* **2017**, *34*, 472−480.

(25) Dalai, N.; Mohanty, B.; Mitra, A.; Jena, B. Highly Active Ternary Nickel–iron oxide as bifunctional catalyst for electrochemical water splitting. *ChemistrySelect* **2019**, *4*, 7791−7796.

(26) Jia, Y.; Zhang, L.; Gao, G.; Chen, H.; Wang, B.; Zhou, J.; Soo, M. T.; Hong, M.; Yan, X.; Qian, G.; Zou, J.; Du, A.; Yao, X. A Heterostructure coupling of exfoliated Ni–Fe hydroxide nanosheet and defective graphene as a bifunctional electrocatalyst for overall water splitting. *Adv. Mater.* 2017, 29, 1700017.

(27) Kumar, A.; Bui, V. Q.; Lee, J.; Jadhav, A. R.; Hwang, Y.; Kim, M. G.; Kawazoe, Y.; Lee, H. Modulating interfacial charge density of NiP_2–FeP_2 via coupling with metallic Cu for accelerating alkaline hydrogen evolution. *ACS Energy Lett.* **2021**, *6*, 354−363.

(28) Shen, B.; Huang, H.; Jiang, Y.; Xue, Y.; He, H. 3D interweaving MXene–graphene network–confined Ni–Fe layered double hydroxide nanosheets for enhanced hydrogen evolution. *Electrochim. Acta* **2022**, *407*, 139913.

(29) Noh, S.; Kim, S.; Le, T.-H.; Heo, E.; Kim, S.; Choi, G. B.; Kim, H.; Kim, Y. A.; Yoon, H. Tuning the microphase behavior of carbon-precursor polymer blends with surfactant-like nanotubes: Toward catalyst support for water splitting. *Chem. Eng. J.* **2022**, *431*, 134027.

(30) Lin, S.; Zhang, T.; Liang, Z. Wet treatment of Ni-containing electroplating wastewater doped with Fe and Co as a hydrogen evolution catalyst. *Energy Fuels* **2022**, *36*, 4107−4117.

(31) Liu, G.; Gao, X.; Wang, K.; He, D.; Li, J. Uniformly mesoporous $NiO/NiFe_2O_4$ biphasic nanorods as efficient oxygen evolving catalyst for water splitting. *Int. J. Hydrogen Energ.* **2016**, *41*, 17976−17986.

(32) Kang, B. K.; Woo, M. H.; Lee, J.; Song, Y. H.; Wang, Z.; Guo, Y.; Yamauchi, Y.; Kim, J. H.; Lim, B.; Yoon, D. H. Mesoporous Ni–Fe oxide multi-composite hollow nanocages for efficient electrocatalytic water oxidation reactions. *J. Mater. Chem. A* **2017**, *5*, 4320−4324.

(33) Yuan, F.; Cheng, X.; Wang, M.; Ni, Y. Controlled synthesis of tubular ferrite MFe_2O_4 (M = Fe, Co, Ni) microstructures with efficiently electrocatalytic activity for water splitting. *Electrochim. Acta* **2019**, *324*, 134883.

(34) Liu, J.; Zhu, D.; Ling, T.; Vasileff, A.; Qiao, S.-Z. S-$NiFe_2O_4$ ultra-small nanoparticle built nanosheets for efficient water splitting in alkaline and neutral pH. *Nano Energy* **2017**, *40*, 264−273.

(35) Lim, D.; Kong, H.; Kim, N.; Lim, C.; Ahn, W.-S.; Baeck, S.-H. Oxygen-deficient $NiFe_2O_4$ spinel nanoparticles as an enhanced electrocatalyst for the oxygen evolution reaction. *ChemNanoMat* **2019**, *5*, 1296−1302.

(36) Wang, K.; Jin, R.; Liu, Y.; Ai, J.; Liu, Z.; Li, X.; Li, N. Three-dimensional ordered macroporous $NiFe_2O_4$ self-supporting electrode with enhanced mass transport for high-efficiency oxygen evolution reaction. *ACS Appl. Energy Mater.* **2021**, *4*, 268−274.

(37) Simon, C.; Timm, J.; Tetzlaff, D.; Jungmann, J.; Apfel, U.-P.; Marschall, R. Mesoporous $NiFe_2O_4$ with tunable pore morphology for electrocatalytic water oxidation. *ChemElectroChem* **2021**, *8*, 227−239.